Asymmetric and connected graphene dimers for a tunable plasmonic response

G. Rosolen* and B. Maes

Micro- and Nanophotonic Materials Group, University of Mons, Place du Parc 20, 7000 Mons, Belgium

(Received 30 August 2015; revised manuscript received 19 October 2015; published 4 November 2015)

We investigate the infrared response of graphene dimers with various doping and polarization configurations. The interaction between the plasmonic resonances of graphene nanodisks leads to a rich, tunable behavior. The hybridization of the nanodisk modes enables the excitation of resonances that would be invisible or dark in a single disk. The simulation results show various anticrossings that depend on dark-bright or bright-bright mode coupling, which we can describe via a simple Hamiltonian model. In addition, we determine the response of a dimer bridged by a tunable graphene junction. This structure leads to charge transfer plasmons, with an even higher absorption efficiency and tunability than nonbridged dimers.

DOI: 10.1103/PhysRevB.92.205405 PACS number(s): 36.40.Mr, 78.67.Wj, 73.20.Mf, 42.25.Bs

I. INTRODUCTION

Metallic nanoparticles with various shapes from spheres to triangles and nanorods have been widely investigated [1–4]. They demonstrate a strong interaction with incident light, with, for example, hot spots on tips, making them suitable for a wide range of applications such as biosensing [5], nonlinear optics [6], nanocircuits [7], and optoelectronics [8]. Strong field enhancements also appear on the edge of two adjacent nanoparticles [9], so that two dipolar modes hybridize and localize the charge density on the junction edges [10]. This hybridization can reveal higher order modes that are not excitable for a single particle [11]. These so-called dark modes become bright thanks to the near-field excitation of the neighboring resonances, as experimentally observed [12,13]. Recently, studies of clusters consisting of even more particles (dimers, trimers, pentamers, etc.) have flourished, in search of hot spots or tunable asymmetric resonances known as Fano resonances [14].

Additionally, dimers were connected by a conductive junction, allowing the charges to oscillate in between the two metallic particles [15]. This creates a new low-energy resonance called a charge transfer plasmon (CTP), which depends on the conductance of the junction and is governed by quantum [16] or classical [17] properties.

However, in metallic clusters, the only effective way to vary the optical response of the system is to change the physical configuration. For example, one needs to vary the size [4], change the metal [15], shift the configuration [18,19], or create a disk-ring nanostructure [20]. This paper expands the work showing that a dimer of graphene disks demonstrates similar phenomena as metallic dimers, but with a strongly tunable absorption efficiency, and shows an interesting intrinsic variation of the mode properties with asymmetric graphene disk doping. This tunability arises from graphene's properties, which can be adjusted via electrical or chemical doping, and leads to a wide range of optical responses [21–25].

Symmetric graphene dimers have been reported before [26–29], but here we discuss the interaction of two graphene disks with different doping levels. This asymmetric dimer structure creates a rather complicated infrared response, as the plasmonic modes hybridize and new resonances appear. Indeed, mode coupling converts dark or subradiant higher order modes into visible, relatively narrow resonances. On the other hand, the coupling of two dipolar, bright resonances can create a subradiant coupled mode, which thus disappears as the doping is tuned.

Furthermore, we investigate graphene dimers connected by a graphene ribbon. The tunable, conductive junction allows charge to oscillate in between the two disks, creating a new narrower and enhanced resonance, the CTP. With metal plasmonics, the conductance of the junction is managed by the size of the junction [17] or the choice of metal [15,30]. Here we show a large tunability of these resonances by exploiting the graphene doping flexibility.

We perform extensive rigorous three-dimensional simulations with COMSOL Multiphysics, a commercial finite-element-based software. In this work the graphene nanodisk parameters are modeled with a surface optical conductivity obtained via the Kubo-Greenwood formula [31,32]:

$$\widetilde{\sigma}_{\text{intra}} = \frac{2ie^2k_BT}{\hbar^2\pi\left(\omega + i\tau_g^{-1}\right)} \ln\left[2\cosh\left(\frac{E_F}{2k_BT}\right)\right], \quad (1)$$

$$\widetilde{\sigma}_{\text{inter}} = \frac{e^2}{4\hbar}\left[\frac{1}{2} + \frac{1}{\pi}\arctan\left(\frac{\hbar\omega - 2E_F}{2k_BT}\right)\right] - \frac{e^2}{4\hbar}\left[\frac{i}{2\pi}\ln\frac{(\hbar\omega + 2E_F)^2}{(\hbar\omega - 2E_F)^2 + (2k_BT)^2}\right], \quad (2)$$

with T the temperature, k_B the Boltzmann constant, and E_F the doping level of graphene. The scattering lifetime of electrons in graphene depends on the doping and is given by $\tau_g = \mu E_F/ev_F^2 \approx 10^{-12}$ s for $E_F = 1$ eV, with the impurity-limited dc conductivity $\mu \approx 10\,000\,\text{cm}^2/(\text{V s})$ and $v_F = 10^6$ m/s the graphene Fermi velocity [33,34]. We operate in the range $\lambda = 3$ to $18\,\mu$m and $E_F = 0$ to 1 eV (Fermi energies up to $E_F = 1$–2 eV have been reported [35]).

Experimental realization of graphene nanodisks has already been achieved [28]. Generally, a graphene sheet is grown using the chemical vapor deposition method [36]. The disks can be protected by nanospheres, while the rest is etched away by oxygen plasma exposure [37]. Local doping can be reached with N-doping of graphene: local N^+ ion irradiation creates vacancy defects in graphene that are filled by N atoms after annealing in NH_3 [38].

*gilles.rosolen@umons.ac.be

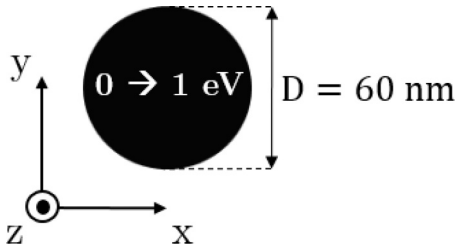

FIG. 1. Scheme of the graphene nanodisk structure, with tunable doping. The incident plane wave is z directed.

Note that finite-size quantum effects are not taken into account in our simulation. Experimental measurements of the extinction cross section of a 50-nm-diameter graphene nanodisk closely correspond with classical simulations [28]. Although a small redshift and broadening of the resonance appears from edge-state damping in zigzag edge configurations [39], the main conclusions of our paper remain. Note, finally, that the 5-nm gap distance between the two nanodisks seems to have no influence on the extinction cross section for either zigzag or armchair configurations. The main contribution to the induced dipole originates from induced charges distributed over regions far from the gap [27].

We first investigate the absorption efficiency of a single graphene nanodisk with various doping levels in Sec. II. This provides for a better understanding of mode hybridization in dimers as described in Sec. III. Finally, we investigate dimers with a conductive junction between the two nanodisks in Sec. IV.

II. SINGLE DISK

In order to develop our methods and prepare our theoretical considerations, we first investigate the absorption efficiency of a free-standing single graphene circular disk of diameter $D = 60$ nm under normal irradiation (z directed; see Fig. 1). Usually, the extinction (sum of absorption and scattering) of the incident electromagnetic field is considered, however, in our case scattering is negligible (by three orders of magnitude), since the nanodisk is small in comparison to the wavelength ($D \ll \lambda_0$) [40]. Therefore, we only consider the absorption efficiency (Q_{abs}) where the absorption (A) is normalized with the irradiance (I) and the surface area ($G = \pi(D/2)^2$),

$$Q_{\text{abs}} = \frac{A}{IG} = \frac{4Ac\mu_0}{|E_0|^2 \pi D^2}, \tag{3}$$

with c the speed of light in vacuum, μ_0 the vacuum permeability, and E_0 the incident electric field [41].

The absorption efficiency of a single disk is plotted in Fig. 2 (logarithmic scale), as a function of doping and the incident wavelength. As demonstrated in previous studies [26,28,40], the dipolar mode (solid red line) dominates and reaches an absorption efficiency of 25, which is 10 times higher than that for conventional metal nanodisks [3]. Another mode appears weakly for a shorter wavelength and lower doping, with an absorption efficiency of $Q_{\text{abs}} \approx 10^{-2}$ (light blue-green line below 0.5 eV). Note that the curve slopes downward for the two modes: indeed, analogous to graphene plasmons, a lower doping implies a smaller imaginary part of the optical

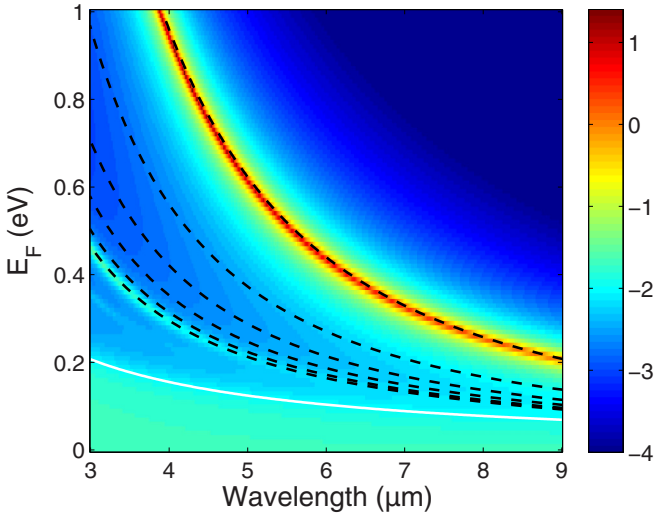

FIG. 2. (Color online) Logarithm of the absorption efficiency (Q_{abs}) for a single nanodisk as a function of the disk doping E_F and incident wavelength. The dipolar mode dominates. A fairly constant absorption appears when graphene is dielectric (below the solid white line). The theoretical dashed black lines represent the first six disk modes.

conductivity of graphene, i.e., a higher effective index or a higher confinement of the field [21,25]. Finally, a fairly constant absorption is observed for doping levels beneath the solid white line. The latter represents the limit $\hbar\omega = 2E_F$: for smaller E_F, interband transitions occur and graphene becomes dielectric, with the well-known value of 2.3% absorption of a graphene sheet [42].

This optical response can be modeled using the Coulomb potential produced by the induced charge density [28,40]. Searching for modes leads to an eigenvalue problem corresponding to a real, unitless value (denoted η_j) for each mode, which depends on the geometrical shape of the graphene flake. Once computed for a mode, the value of η_j is then fixed: a change in the graphene conductivity (via doping, for example) will imply a variation of the disk diameter D or the frequency ω, via

$$\eta_j = \frac{i\sigma(\omega, E_F)}{4\pi\varepsilon_0\omega D}, \tag{4}$$

with ε_0 the vacuum permittivity. In Fig. 3 we show the various mode profiles with the corresponding η_j value, with j numbering the mode. The mode profiles are the total charge density computed using the time-harmonic current continuity equation $\rho = -\vec{\nabla}\cdot\vec{J}/(i\omega)$, with $\vec{J}$ the current density. We mainly observe a linear charge on the edge for the dipolar mode (mode 0), with more charge appearing on the surface for higher order modes. The sixth mode (mode 5) is a higher order dipolar mode and shows a radial node. Note that the first mode value ($\eta_0 = 0.07$) matches the theoretical value of a perfect conductor disk [43] [$\eta_0 = (3\pi^2/2)^{-1} = 0.07$] and a previous study of graphene disk resonances [28] ($\eta_0 = 0.08$).

This fundamental parameter η_j is determined after computing the resonant frequency once for a fixed (but fairly arbitrary) $E_F = 0.4$ eV with the COMSOL eigenfrequency solver. With the η_j value we easily determine the resonant frequency for

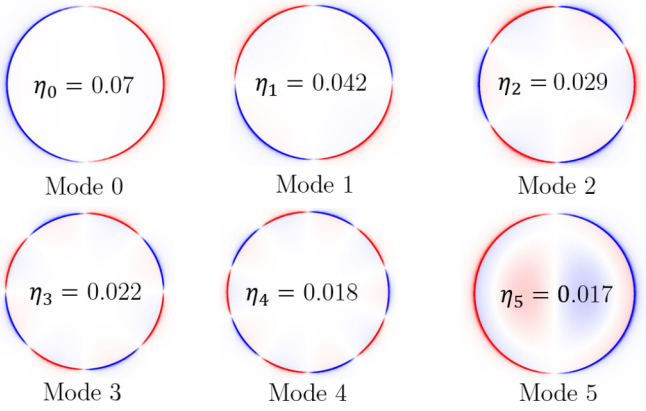

FIG. 3. (Color online) First six mode profiles (charge distribution) of the graphene nanodisks with their corresponding η_j eigenvalue.

the particular mode for all doping levels, using Eq. (4). In this way the mode dispersions of the first six modes are plotted by dashed black lines in Fig. 2, in good agreement with the full simulations. One observes that only the dipolar modes (modes 0 and 5) couple with the incident electric field; all the other modes are dark due to the incompatibility of their symmetry with the excitation. In order to excite these dark modes, we need to employ asymmetric dimers, as in the following section.

III. GRAPHENE DIMERS

We demonstrate that a free-standing graphene dimer gives rise to a more complicated pattern of absorption when the doping is tuned judiciously. Indeed, the modes of the two disks hybridize and give rise to various anticrossing effects. We examine a 60-nm-diameter disk with 0.4-eV doping, placed at a 5-nm distance from a second disk with doping varying from 0 to 1 eV (see Fig. 4). We investigate two directions of polarization of the incident electric field: parallel (x directed; Sec. III A) and perpendicular (y directed; Sec. III B). The incidence direction remains perpendicular to the disk planes (along the z axis).

A. Parallel polarization

The absorption efficiency as a function of the wavelength and doping is plotted in Fig. 5 for x-directed electric-field excitation. The first observation is the increase in the complexity

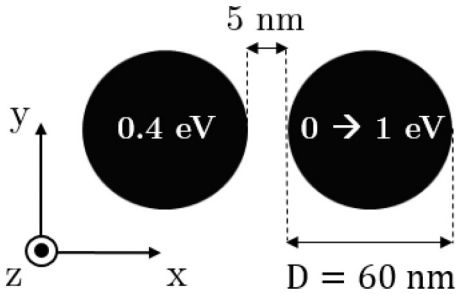

FIG. 4. Graphene dimer with one disk of 0.4-eV doping and the other of varying doping. Normal incidence along the z direction.

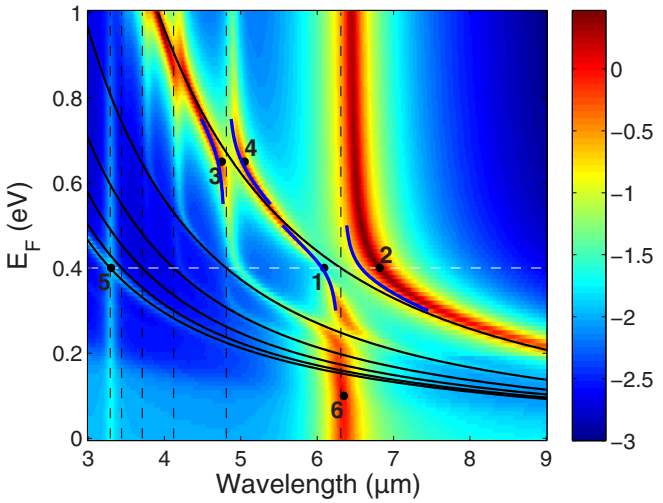

FIG. 5. (Color online) Logarithm of the absorption efficiency of a graphene dimer with a fixed 0.4-eV disk and a varyingly doped disk (from 0 to 1 eV) as a function of the wavelength for x polarization. Solid black lines represent the first six modes, with varying doping; dashed vertical lines, 0.4 eV. The dashed horizontal white line indicates equally doped disks. Short, thick solid (blue) lines are from perturbation theory.

of the absorption pattern in comparison with the single-disk absorption efficiency (Fig. 2). Solid black lines represent the first six modes of a single disk (with varying E_F values) as explained in Sec. II, and dashed vertical lines are for a fixed 0.4-eV-doped disk. We observe a superposition and interaction of these modes. The fundamental dipolar modes (mode 0 in Fig. 3) of the two disks dominate the spectra, but complexity appears where modes cross, e.g., around points 1 and 2 and around points 3 and 4, which gives rise to anticrossings of a different nature, as we will discuss.

The particular shape of the anticrossing bands can be described with a classical model of two coupled oscillators [44]. The correspondence between energy level E and resonant wavelength λ_r is $E = 2\pi c\hbar/\lambda_r$. With E_i (E_v) the energy level of a single-disk mode with invariant $E_F = 0.4$ eV (varying E_F), corresponding to the dashed black (solid black) lines in Fig. 5. The perturbed Hamiltonian of the model is

$$\widehat{H} = \widehat{H}_0 + \widehat{W} = \begin{pmatrix} E_i + W_{11} & W_{12} \\ W_{21} & E_v + W_{22} \end{pmatrix}, \qquad (5)$$

with $\widehat{W}$ the perturbation via coupling of disks. For simplicity, we suppose a nondiagonal perturbation matrix ($W_{11} = W_{22} = 0$) and reciprocal coupling ($W_{12} = W_{21} = \Delta$). The eigenvalues of the coupling problem $\widehat{H}\Psi = E_\pm\Psi$ are then [45]

$$E_\pm = \tfrac{1}{2}(E_i + E_v) \pm \tfrac{1}{2}\sqrt{(E_i - E_v)^2 + 4\Delta^2}. \qquad (6)$$

The only undetermined parameter Δ can be fitted to follow the particular anticrossing pattern. The results of this perturbation theory are plotted by short, thick solid (blue) lines for two anticrossings in Fig. 5, as discussed below.

First, we describe the interaction between the two dipolar modes of similar doping, $E_F = 0.4$ eV (around $\lambda_0 = 6.5\,\mu$m). This is the particular case of the bonding and antibonding dipolar dimer plasmon [17]; we observe an anticrossing

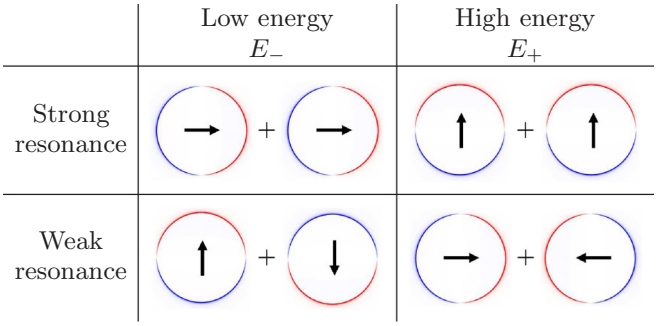

FIG. 6. (Color online) Possible linear combinations of the dipolar modes for parallel (horizontal) and perpendicular (vertical) polarizations. Arrows indicate the dipolar moment directions of the involved single-disk resonances.

between two dipolar single-disk modes. The coupling Δ between these two modes lifts the degeneracy and we obtain two solutions [short, thick solid (blue) curves in Fig. 5]: E_+ (at the left; shorter wavelengths) and E_- (at the right). Here, we fit $\Delta = 20$ meV and take the single-disk resonances $E_i = 0.20$ eV and E_v varying from 0.17 to 0.22 eV. The short, thick solid (blue) curves correctly follow the absorption pattern but are blueshifted: this is due to the approximation $W_{11} = W_{22} = 0$. In the simulations the mode wavelengths redshift with the interaction of the neighboring disk. This redshift is general and is shown in Fig. 5 as the dashed vertical lines do not perfectly fit the simulated absorption pattern.

The resulting mode is a linear combination of the two (nearly) identical dipolar modes (mode 0 in Fig. 3). The two possible combinations are illustrated in Fig. 6 for parallel polarization (horizontal arrows). The lower energy mode combination corresponds to E_- and to a strong resonance since the dipolar moments are parallel (top-left in Fig. 6) [10]. On the other hand, the other combination requires a higher energy (E_+), as the dipolar moments are opposed, resulting in a zero total dipolar moment (bottom-right in Fig. 6). Due to the symmetry of the excitation, the latter mode is dark in our spectrum, which explains the lack of resonance at point 1 in Fig. 5 and the strong resonance at point 2. This is further supported by the plot of the corresponding field enhancement in Figs. 7(1) and 7(2): they are both identically scaled in order to distinguish the dark mode (1) from the bright mode (2).

Second, we describe the anticrossing of two qualitatively different modes: the dipolar mode of the 0.65-eV-doped disk and the quadrupolar mode of the 0.4-eV-doped disk (points 3–4 around 5 μm in Fig. 5). The short, thick solid (blue) curves for perturbation theory are plotted in this area and follow the absorption pattern. In this case $\Delta = 8$ meV, indicating a smaller coupling with higher order modes (compared to 10 meV of dipolar-dipolar interaction): the charge density on the edge near the other disk is lower for the quadrupolar mode, as charges are more distributed (see mode 1 in Fig. 3). For this coupling, the normally dark quadrupolar mode (no coupling in Fig. 2) becomes bright over a large E_F range thanks to the evanescent field of the neighboring dipolar mode. At the crossing point, we then observe the quadrupolar resonance (point 3 in Fig. 5) as can be seen by the enhancement of the electric field in Fig. 7(3) and the dipolar mode (point 4 in Fig. 5) represented in Fig. 7(4). Note that we still observe the redshift of the modes as explained previously.

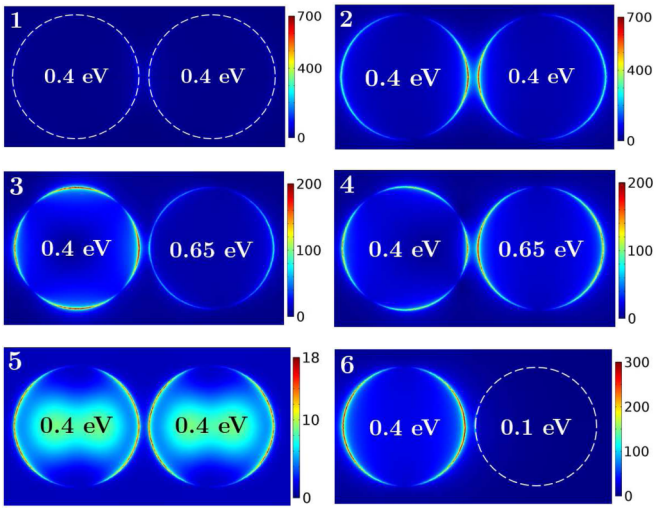

FIG. 7. (Color online) Enhancement of the electric field (total electric field over incident electric field, $|E|/|E_0|$) for particular points in Fig. 5. Dashed white circles represent the edge of the graphene disk when there is no resonance. Plot numbers indicate the points in Fig. 5.

Furthermore, the sixth mode for each disk is (weakly) visible in Fig. 5: the dashed vertical line around $\lambda_0 = 3.3$ μm and the lowest black curve. At their crossing (around point 5) the modes are not perturbed (Δ negligible) and do not interact as suggested by the electric-field enhancement [Fig. 7(5)]. Indeed, the evanescent field at the edges demonstrates a faster decay than the lower order modes.

Finally, the charge density profile of point 6 in Fig. 5 is depicted in Fig. 7(6). At this wavelength ($\lambda_0 = 6.35$ μm), the 0.1-eV-doped graphene disk (at right) is dielectric, and the incident electric field only couples with the dipolar mode of the fixed 0.4-eV-doped graphene disk.

B. Perpendicular polarization

In this section we briefly discuss perpendicular y-directed electric-field polarization (Fig. 4), with the absorption efficiency in Fig. 8. Again, the first six modes of single disks are represented by a solid (varying E_F) or dashed black ($E_F = 0.4$ eV) line.

Generally, one observes a smaller influence of the second disk than in the previous section. First, there is no redshift of the modes in this case. Second, the anticrossings are less pronounced. For example, the dipolar-dipolar anticrossing around 0.4 eV and $\lambda_0 = 6.3$ μm shows a coupling of $\Delta = 4.5$ meV, twice as small as the $\Delta = 10$ meV for parallel polarization (Sec. III A). The quadrupolar-dipolar anticrossing (around 0.65 eV and 4.8 μm) is also characterized by a weak coupling of $\Delta = 4$ meV. Indeed, with perpendicular polarization the charge densities are not as concentrated at the edge of the small gap between the two disks (Fig. 6, top-right and bottom-left), reducing the influence of the neighboring disk and explaining the better fit between single-disk resonances and the simulated dimer absorption.

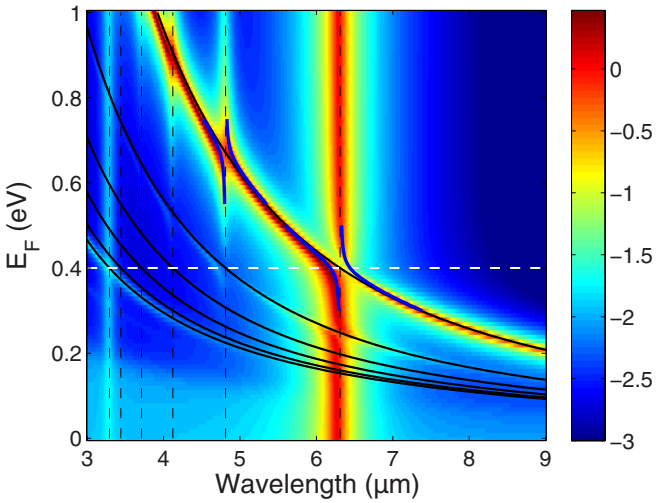

FIG. 8. (Color online) Logarithm of the absorption efficiency of a graphene dimer with a fixed 0.4-eV disk and a varyingly doped disk (from 0 to 1 eV) as a function of the wavelength for y polarization. Solid black lines represent the first six modes, with varying doping; dashed vertical lines, 0.4 eV. The dashed horizontal white line indicates equally doped disks. The thickest solid (blue) lines are from perturbation theory.

We focus now on an anticrossing of dipolar-dipolar modes (at $\lambda_0 = 6$ to 7 μm and around $E_F = 0.4$ eV). An important difference appears in comparison to the parallel polarization case in Fig. 5. In perpendicular polarization the bright resonance occurs at a high energy (short wavelength), while the dipolar moments cancel at a low energy. In this case, the resonant energy is lower when the charge oscillates out of phase (see Fig. 6) and the dark mode therefore appears on the right (higher wavelength) side of the anticrossing.

IV. TUNABLE CHARGE TRANSFER DIMER

An alternative way to induce a tunable response is to introduce a charge transfer component. This consists, e.g., in a graphene bridge connecting the two disks, which allows electric charges to oscillate from one disk to the other: the CTP. It was demonstrated that the CTP properties for metals strongly depend on the junction conductance [17]. Graphene is therefore a very suitable CTP material due to its tunable conductivity.

Here, we examine two graphene disks (diameter $D = 60$ nm) separated by a distance of 15 nm and with the same doping (0.4 eV). We add a charge transfer junction 25 nm wide (see Fig. 9; classical electromagnetic simulations are accurate for ribbons wider than about 25 nm [33]).

In this system we vary the junction conductance via the graphene doping, from 0.4 to 1 eV. The absorption is plotted in Fig. 10 for the wavelength range 4–18 μm. The hybridized nonbridged dipolar-dipolar resonance around $\lambda_0 = 6.5$ μm is also shown for comparison (dashed line). Note that the maximal absorption efficiency is lower than previously, due to the longer distance $d = 15$ nm between the two nanodisks ($d = 5$ nm in Sec. III).

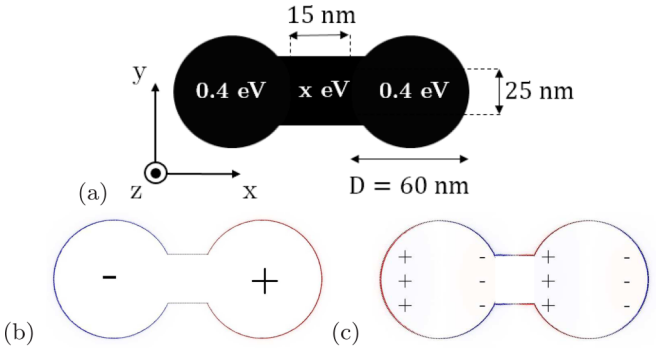

FIG. 9. (Color online) (a) Scheme of the charge transfer structure. Charge density of the 0.4-eV-doped junction for (b) a CTP at $\lambda_0 = 14.3$ μm and (c) a screened bonding dipolar plasmon at $\lambda_0 = 5.7$ μm.

When the dimer is bridged, two groups of resonances are distinguished: one is redshifted, while the other group appears at shorter wavelengths. The redshifted resonances are the CTPs; the particular oscillation of the electrons between the disks is presented in Fig. 9(b): one disk is a positive pole and the other a negative pole. This is completely different from Sec. III, where the charges oscillate separately on each disk (Fig. 6). With the junction the dimer acts as a continuous particle of longer length, which consequently induces a redshift. The magnitude of the redshift depends on the time needed for the electrons to cross the junction, which is inversely proportional to the conductance [17]. In our case the only varying factor is the conductivity, as the junction size is invariant. This explains why 1-eV-doped graphene (higher conductivity) resonates at a shorter wavelength than lightly doped graphene junctions. Note, finally, that the peak is narrower for higher doping, i.e., better conductivity. Indeed, a simple resistor model shows that decreasing the conductivity increases the dissipation in the junction (as the electron

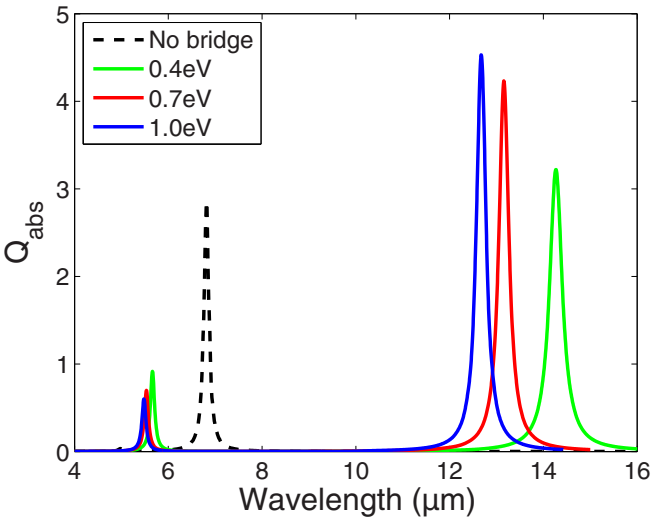

FIG. 10. (Color online) Absorption efficiency of a graphene charge transfer dimer with varying bridge doping. The nonbridged dipolar-dipolar resonance is plotted as the dashed black line for comparison.

scattering lifetime decreases) and therefore broadens the CTP resonance [17].

The blueshifted family of resonances is called the screened bonding dipolar plasmon [30]. The nonbridged dipolar-dipolar resonance, which is a capacitive coupling over the dimer gap, is screened by the charge transfer, inducing a blueshift and a weaker absorption efficiency. The charge densities are plotted in Fig. 9(c) for 0.4-eV doping throughout. The dipolar modes of the two nanodisks are still visible, as charge also appears on the edges of the junction. In the case of lower doping, the resistance in the junction increases, reducing the screening and therefore the blueshift.

V. CONCLUSION

In conclusion, we simulate the infrared response of asymmetric graphene dimers, induced by different doping levels, leading to an intricate and tunable absorption spectrum. We demonstrate mode hybridization, with dark modes becoming bright, and vice versa. This leads to qualitatively different anticrossing levels, which can be modeled with standard perturbation methods.

Finally, we demonstrate strong and tunable absorption efficiencies with CTP resonances when the graphene disks are coupled via a bridge of varying doping. These numerical considerations of junctions show their interest for ease of tunability: with conventional metals the optical properties are only adjusted when the metal of the junction is exchanged for another metal. Further investigations can consider, e.g., particular nonuniform graphene doping profiles of the junction. Our findings could lead to molecular junction conduction measurements, since standard electrical transport measurements cannot be performed in gigahertz and higher frequency regimes due to the strong capacitive coupling between electrodes [17]. Moreover biosensors could be designed by providing a molecular functionalization of the graphene junction.

Further work can also examine more complicated cluster structures, such as pentamers, where tunable responses should also appear. Other studies suggest the potential for Fano resonances [14,18] when the symmetry is broken by the size or the position of the center particle. Graphene nanodisk pentamers could deliver a similar response simply by adjusting the doping level of the central disk.

ACKNOWLEDGMENTS

This work was supported by the Belgian Science Policy Office under the project Photonics@be (P7-35) and by the Fonds De La Recherche Scientifique (F.R.S.-FNRS), Belgium.

[1] S. Viarbitskaya, A. Teulle, R. Marty, J. Sharma, C. Girard, A. Arbouet, and E. Dujardin, Nat. Mater. **12**, 426 (2013).
[2] E. Prodan, C. Radloff, N. J. Halas, and P. Nordlander, Science **302**, 419 (2003).
[3] M. K. Krug, M. Reisecker, A. Hohenau, H. Ditlbacher, A. Trgler, U. Hohenester, and J. R. Krenn, Appl. Phys. Lett. **105**, 171103 (2014).
[4] Z. Liao, B. C. Pan, X. Shen, and T. J. Cui, Opt. Express **22**, 15710 (2014).
[5] J. N. Anker, W. P. Hall, O. Lyandres, N. C. Shah, J. Zhao, and R. P. Van Duyne, Nat. Mater. **7**, 442 (2008).
[6] M. A. van der Veen, G. Rosolen, T. Verbiest, M. K. Vanbel, B. Maes, and B. Kolaric, J. Mater. Chem. C **3**, 1576 (2015).
[7] N. Engheta, Science **317**, 1698 (2007).
[8] F. Bonaccorso, Z. Sun, and A. Ferrari, Nature Photon. **4**, 611 (2010).
[9] I. Romero, J. Aizpurua, G. W. Bryant, and F. J. García de Abajo, Opt. Express **14**, 9988 (2006).
[10] P. Nordlander, C. Oubre, E. Prodan, K. Li, and M. I. Stockman, Nano Lett. **4**, 899 (2004).
[11] Z.-J. Yang, Z.-S. Zhang, L.-H. Zhang, Q.-Q. Li, Z.-H. Hao, and Q.-Q. Wang, Opt. Lett. **36**, 1542 (2011).
[12] S.-C. Yang, H. Kobori, C.-L. He, M.-H. Lin, H.-Y. Chen, C. Li, M. Kanehara, T. Teranishi, and S. Gwo, Nano Lett. **10**, 632 (2010).
[13] A. Abass, S. R.-K. Rodriguez, J. Gomez Rivas, and B. Maes, ACS Photon. **1**, 61 (2014).
[14] B. Luk'yanchuk, N. I. Zheludev, S. A. Maier, N. J. Halas, P. Nordlander, H. Giessen, and C. T. Chong, Nat. Mater. **9**, 707 (2010).
[15] F. Wen, Y. Zhang, S. Gottheim, N. S. King, Y. Zhang, P. Nordlander, and N. J. Halas, ACS Nano **9**, 6428 (2015).
[16] S. Thongrattanasiri, A. Manjavacas, P. Nordlander, and F. J. García de Abajo, Laser Photon. Rev. **7**, 297 (2013).
[17] O. Perez-Gonzalez, N. Zabala, A. G. Borisov, N. J. Halas, P. Nordlander, and J. Aizpurua, Nano Lett. **10**, 3090 (2010).
[18] M. Rahmani, B. Lukiyanchuk, B. Ng, A. Tavakkoli K. G., Y. F. Liew, and M. Hong, Opt. Express **19**, 4949 (2011).
[19] W. Wang, T. Christensen, A.-P. Jauho, K. S. Thygesen, M. Wubs, and N. A. Mortensen, Sci. Rep. **5**, 9535 (2015).
[20] J. Li, T. Liu, H. Zheng, J. Dong, E. He, W. Gao, Q. Han, C. Wang, and Y. Wu, Plasmonics **9**, 1439 (2014).
[21] M. Jablan, H. Buljan, and M. Soljacic, Phys. Rev. B **80**, 245435 (2009).
[22] Y. Yao, M. Kats, P. Genevet, N. Yu, Y. Song, J. Kong, and F. Capasso, Nano Lett. **13**, 1257 (2013).
[23] T. Low and P. Avouris, ACS Nano **8**, 1086 (2014).
[24] G. Rosolen and B. Maes, J. Opt. Soc. Am. A **31**, 1096 (2014).
[25] G. Rosolen and B. Maes, J. Opt. **17**, 015002 (2015).
[26] S. Thongrattanasiri, F. H. L. Koppens, and F. J. García de Abajo, Phys. Rev. Lett. **108**, 047401 (2012).
[27] S. Thongrattanasiri and F. J. García de Abajo, Phys. Rev. Lett. **110**, 187401 (2013).
[28] Z. Fang, S. Thongrattanasiri, A. Schlather, Z. Liu, L. Ma, Y. Wang, P. M. Ajayan, P. Nordlander, N. J. Halas, and F. J. García de Abajo, ACS Nano **7**, 2388 (2013).
[29] M. V. Balaban, O. V. Shapoval, and A. I. Nosich, J. Opt. **15**, 114007 (2013).
[30] L. Liu, Y. Wang, Z. Fang, and K. Zhao, J. Chem. Phys. **139**, 064310 (2013).
[31] L. Falkovsky and A. Varlamov, Eur. Phys. J. B **56**, 281 (2007).
[32] L. Falkovsky, J. Phys.: Conf. Ser. **129**, 1 (2008).
[33] J. Christensen, A. Manjavacas, S. Thongrattanasiri, F. H. L. Koppens, and F. J. García de Abajo, ACS Nano **6**, 431 (2012).

[34] K. S. Novoselov, A. K. Geim, S. V. Morozov, D. Jiang, Y. Zhang, S. V. Dubonos, I. V. Grigorieva, and A. A. Firsov, Science **306**, 666 (2004).
[35] D. K. Efetov and P. Kim, Phys. Rev. Lett. **105**, 256805 (2010).
[36] X. Li, W. Cai, J. An, S. Kim, J. Nah, D. Yang, R. Piner, A. Velamakanni, I. Jung, E. Tutuc *et al.*, Science **324**, 1312 (2009).
[37] X. Zhu, W. Wang, W. Yan, M. B. Larsen, P. Boggild, T. G. Pedersen, S. Xiao, J. Zi, and N. A. Mortensen, Nano Lett. **14**, 2907 (2014).
[38] B. Guo, Q. Liu, E. Chen, H. Zhu, L. Fang, and J. R. Gong, Nano Lett. **10**, 4975 (2010).
[39] T. Christensen, W. Wang, A.-P. Jauho, M. Wubs, and N. A. Mortensen, Phys. Rev. B **90**, 241414 (2014).
[40] F. J. García de Abajo, ACS Photon. **1**, 135 (2014).
[41] C. F. Bohren and D. R. Huffman, *Absorption and Scattering of Light by Small Particles* (Wiley-VCH Verlag, Weinheim, Germany, 2007), pp. 57–81.
[42] R. Nair, P. Blake, A. N. Grigorenko, K. Novoselov, T. Booth, T. Stauber, N. M. R. Peres, and A. Geim, Science **320**, 1308 (2008).
[43] H. C. van de Hulst, *Light Scattering by Small Particles*, *States of Matter Series* (Dover, Mineola, NY, 1981).
[44] F. Liu and E. Cubukcu, Phys. Rev. B **88**, 115439 (2013).
[45] C. Cohen-Tannoudji, B. Diu, and F. Laloe, *Quantum Mechanics, Vol. 1* (Wiley, New York, 1977).